



Deposited via The University of Leeds.

White Rose Research Online URL for this paper:

<https://eprints.whiterose.ac.uk/id/eprint/128464/>

Version: Accepted Version

Article:

Wei, L, Magee, DR and Cohn, AG (2018) An anomalous event detection and tracking method for a tunnel look-ahead ground prediction system. *Automation in Construction*, 91. pp. 216-225. ISSN: 0926-5805

<https://doi.org/10.1016/j.autcon.2018.03.002>

Copyright (c) 2018 Elsevier B. V. Licensed under the Creative Commons Attribution-Non Commercial No Derivatives 4.0 International License (<https://creativecommons.org/licenses/by-nc-nd/4.0/>)

Reuse

This article is distributed under the terms of the Creative Commons Attribution-NonCommercial-NoDerivs (CC BY-NC-ND) licence. This licence only allows you to download this work and share it with others as long as you credit the authors, but you can't change the article in any way or use it commercially. More information and the full terms of the licence here: <https://creativecommons.org/licenses/>

Takedown

If you consider content in White Rose Research Online to be in breach of UK law, please notify us by emailing eprints@whiterose.ac.uk including the URL of the record and the reason for the withdrawal request.

An Anomalous Event Detection and Tracking Method For A Tunnel Look-ahead Ground Prediction System

Lijun Wei, Derek R. Magee, Anthony G. Cohn

School of Computing, University of Leeds, United Kingdom

Abstract

The complicated geological conditions and unexpected geological hazards beyond the face of a tunnel are challenging problems for tunnel construction, which can cause great loss of life and property. While the geological surveys conducted before tunnel construction can provide rough information of construction site, they are not sufficiently accurate for predicting the sudden geological condition changes in local areas. Within the EU NETTUN project, an on-board ground prediction system consisting of multiple ground penetrating radars (GPR) and seismic sensors were developed to “see through” the ground and provide the local ground information behind the excavation front surface of a TBM (Tunnel Boring Machine). In order to facilitate the interpretation of the imaging data captured by this system, an automatic event detection and tracking method is presented in this paper. Anomalous 2D features are detected on each radar profile and reconstructed into a 3D accumulator; then, probable 3D events are detected from the accumulator and tracked at subsequent locations based on the information from multiple sets of radar data. The detection results can be used to generate alarms or be sent to human operators for interactive interpretation. The proposed method was evaluated using two sets of GPR data captured in a designed test field. Experimental results show that the buried targets can be correctly detected by the proposed event detection and tracking method. The proposed method is sufficiently flexible to cope with variations on the spatial configuration of on-board sensors.

Keywords: GPR data; Event detection; Tunnel construction; Ground prediction system

1. Introduction

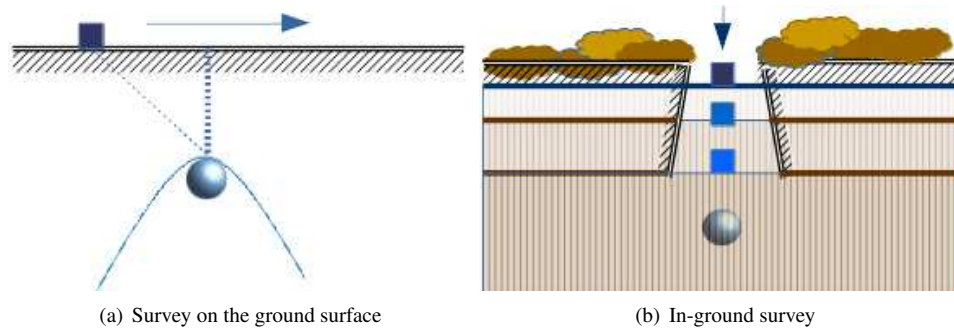
The complicated geological conditions and geological hazards are challenging problems for tunnel construction, which can cause great loss of life and property. For example, large obstacles like boulders, building foundations, archaeological remains and other tunnels can obstruct the digging; geological defective features like cavities, sudden ground changes (e.g. from gravel to fractured rock), groundwater in adverse geological bodies (e.g. faults, karst caves and coal mine collapse column) [1] can also make the construction dangerous. While geological surveys conducted before the tunnel construction can provide rough information of the construction site, they are not sufficiently accurate for predicting the sudden geological condition changes in local areas. In order to improve the safety and efficiency in tunnelling, geophysical sensors and computer algorithms have been proposed or applied to predict the ground conditions ahead the excavation front surface such that appropriate ground treatment and effective support installation can be conducted. Probabilistic models like neural network [2], Markov random process [3] were proposed to dynamically predict the ground conditions based on the excavated ground data. These methods are useful for determining the short range geology ahead the tunnel face. In addition

to these, tunnel look-ahead ground prediction systems (Figure 1), equipped with different types of on-board ground probing/imaging geophysical techniques, have also been proposed for predicting the ground conditions [4, 5], such as tunnel seismic prediction (TSP) method [6], electrical resistivity method [7], transient electromagnetic method (TEM) [4] and ground penetrating radar (GPR) method [8, 9]. These systems can help assess the local geology conditions a few metres ahead of the excavation front surface. An overview of the existing tunnel look-ahead geological prospecting systems in tunnelling construction was given by Li et al. in [10].

Currently, most existing ground prediction systems require stopping tunnel construction activities for several hours so experts can install sensors on tunnel front surface/side walls or to drill a borehole through the tunnel front to insert measurement devices. These works usually lead to delay of tunnel construction. For tunnels constructed using a TBM (Tunnel Boring Machine), an on-board ground prediction system with the functionality of automated data acquisition/storage, 3D visualisation, human-machine interactive interpretation and a direct communication with the TBM operator can potentially make the drilling operation safer and even increase the excavation speed. A prototype of such a system, named Tunnel Look-ahead Imaging Prediction System (TULIPS) [11, 12] has been developed within the EU NETTUN project ¹.

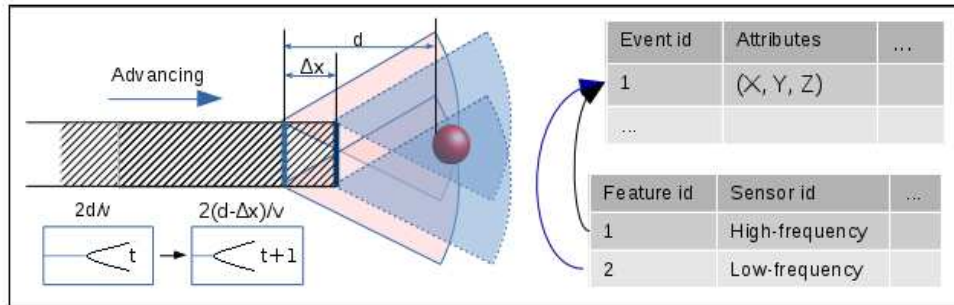
Email address: L.J.Wei@leeds.ac.uk, D.R.Magee@leeds.ac.uk, A.G.Cohn@leeds.ac.uk; (Lijun Wei, Derek R. Magee, Anthony G. Cohn)

¹<http://nettun.org/>



(a) Survey on the ground surface

(b) In-ground survey



(c) (Left) In-tunnel survey for ground inspection with multiple sensors. (Right) Anomalous features detected by different sensors are associated to the same event.

Figure 1: A detailed illustration of continuous survey for tunnelling construction prospecting. The sensing devices are pushed forward and are getting closer and closer to the targets. Anomalous features are detected from sensor data captured at consecutive locations and associated to the corresponding event.

49 The TULIPS system consists of multiple sets of GPR antennae of different frequencies as well as a seismic imaging system.
50 There are three sets of complementary GPR antennae on TULIPS: a low frequency GPR to provide a large inspection
51 operating range and two high frequency GPR sensors to detect small-sized targets like rock fractures which might be a
52 few centimetres in length. The imaging system is placed on three different radii sequentially (along an arm), and on each
53 radius the system is rotated in an anti-clockwise direction with a constant rate to collect data, so each GPR sensor can provide
54 one data set per radius and three sensors can generate nine images in total which can guarantee the best coverage of the space
55 in front of the ground prediction system[11]. Examples of the generated three images by a GPR sensor are shown in Fig. 2
56 (left). The ground prediction system is designed to be installed in front of a TBM cutter head, so the imaging process is repeated
57 each time a tunnel segment ring is being erected along the tunnel axis. An anomalous target detection method has been
58 proposed for this system by Wang et al. in [12], in which GPR data is preprocessed to remove noise, then back-projected into
59 3D for analysis. However, in practice, the surrounding ground could be heterogeneous so the received signal strength (GPR
60 image intensity) could vary in different parts of a GPR image. Directly projecting the image pixel intensities into 3D may not
61 help reveal the targets in areas which are relatively challenging for GPR sensors.
62
63
64
65
66
67
68
69
70
71
72
73
74

75 Therefore, in this paper, an automatic event detection and tracking method is proposed for detecting and tracking anomalous
76

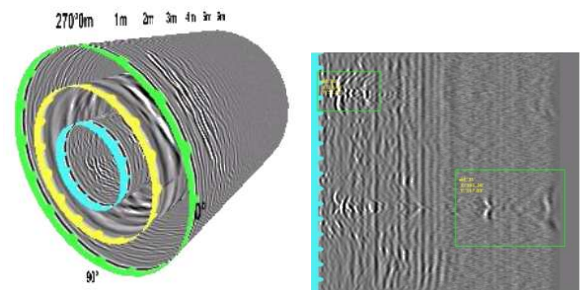


Figure 2: (Left) Example of three circular GPR images captured by a GPR sensor on TULIPS; (right) Planar view of the GPR image on the innermost radius. The detected anomalous regions are marked by green boxes (For interpretation of the references to colour in this figure legend, the reader is referred to the electronic version of this article).

77 lous 3D events from the GPR data acquired by this system. Potential features are first analysed in local image regions by
78 examining the dissimilarity of a pixel to its surroundings. Then the obtained feature maps are back-projected into a 3D accumulator
79 for analysis. As the detections from a single image profile may not guarantee the existence nor indicate the type/size of a
80 target, the data fusion step correlates all information sets from different GPR sensors at different radii and subsequent tunnel
81 locations in 3D. When the sensor platform moves forward, a 3D target tracking scheme is applied for consistently tracking
82 the targets from frame to frame. Then these corresponding 3D
83
84
85
86
87

88 targets are re-projected to individual GPR images as the final
 89 anomalous 2D features. Information of the detected 3D events and
 90 and the associated 2D image features are stored in a database and
 91 can be visualised to TBM-operator to facilitate the interpre-
 92 tation by geo-experts. The processing pipeline of the proposed
 93 event detection and tracking method is shown in Figure 3.



Figure 3: Pipeline of the proposed event detection and tracking method.

94 The remaining sections of this paper are organized as fol-
 95 lows: detection of potential features in individual images is in-
 96 troduced in Section 2, then the data fusion and events identifi-
 97 cation/tracking method is presented in Section 3, followed by
 98 experimental results in Section 4 and conclusions in Section 5.

99 2. Detection of Potential Features in Ground Penetrating 100 Radar data

101 The objective of this step is to identify potential anomalous
 102 features in individual GPR images. Features are local changes
 103 in the sensor data which could indicate the presence of an
 104 “event” in the physical world, such as geology events (e.g. fault,
 105 karst) and anthropic structures (e.g. building foundation, pipes).
 106 As areas in GPR images with large intensity (except those from
 107 ground echo and noise) are generally relating to the reflections
 108 from underground objects with high dielectric contrast to the
 109 surrounding medium, a GPR image is usually separated into
 110 background and foreground (interesting) regions using intensity
 111 based thresholding methods [13], i.e. background is related to
 112 the areas without obvious/strong signal reflections, and regions
 113 of interest are areas with stronger signal reflections. A com-
 114 parison of three types of thresholding methods for interesting
 115 region extraction is given in experimental section 5.

116 In this work, instead of considering each GPR image pixel
 117 separately, features are considered as local pixels/regions with
 118 different intensities with respect to their local neighbouring ar-
 119 eas according to image local statistics [14, 15, 16]. After apply-
 120 ing the common preprocessing steps on a raw GPR image (i.e.,
 121 signal de-wow correction, programmed gain control, horizontal,
 122 filter, bandpass filter and time/depth correction) using an IDS,
 123 standard processing software², a 3×3 median filter is applied
 124 to the GPR image to remove background noise, followed by
 125 subtracting the average of each horizontal trace from all traces,
 126 to remove ground echo. Then, the potential feature map is cal-
 127 culated based on the image Laplacian pyramid by comparing
 128 the sub-sampled images in different scales.

129 As shown in Figure 4, an input GPR image is firstly sub-
 130 sampled to s resolutions as I_s , $s \in [S_1, S_2, S_3 \dots, S_m]$, such

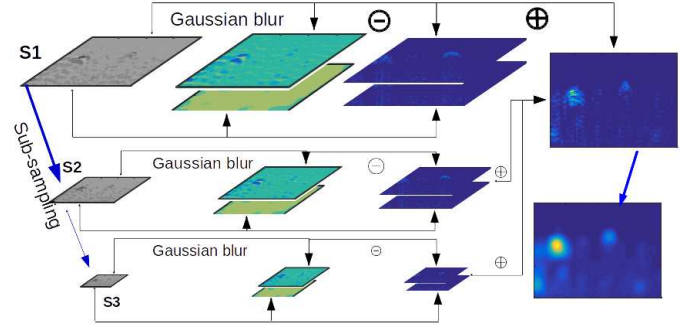


Figure 4: Feature extraction method from individual GPR image.

Algorithm 1 Extraction of potential features in a radar image I

```

1: for  $s \in [S_1, S_2, S_3 \dots, S_m]$  do
2:    $I_s :=$  sub-sample image  $I$  with scale  $s$ 
3:   for  $\sigma = [2, 8]$  do
4:      $I_s^\sigma :=$  convolve  $I_s$  with Gaussian filter  $g(\sigma)$ 
5:   end for
6:    $I_s^d := \text{norm}(\sum_{\sigma} \|I_s - I_s^\sigma\|)$ 
7:    $I_s^d :=$  resize  $I_s^d$  to the size of input image  $I$ 
8:    $I_s^{\text{min}} :=$  find the average of local maxima in  $I_s^d$ 
9:    $p^s :=$  calculate the weight of  $I_s$  using  $(1 - I_s^{\text{min}})^2$ 
10: end for
11:  $I_{\text{out}} = \sum_s p^s * I_s^d$ 

```

as $[1/2, 1/4, 1/8]$. Each pixel in the higher level of a pyra-
 mid contains the local average of its pixel neighbourhood on a
 lower level image. In order to find regions with different ampli-
 tude to their surroundings, each sub-sampled image is blurred
 using a set of Gaussian filters with different standard deviations
 (σ_1, σ_2) . Differences of the Gaussian-blurred images with re-
 spect to the original sub-sampled image are summed up and
 normalized as I_s^d to represent the dissimilarity of pixels with
 their surroundings in the current scale. The weighted sum of I_s^d
 at different image scales is used as the image intensity feature
 map. The algorithm is given in Algorithm 1. This step is ap-
 plied to images from different imaging sensors (low frequency
 and high frequency GPR) on different radii, and data captured at
 subsequent locations. The extracted pixels and their associated
 values are sent forward to the next fusion stage.

3. Integration of the Feature Maps from Multiple Sensors in A 3D Accumulator for Event Identification

By assuming that the tunnel is locally linear, the space ahead
 of the tunnel construction face is discretized into a 3D voxel
 grids, which are used as an accumulator to store the “possibil-
 ity” of each grid being occupied by potential anomalous events.
 With the locations of on-board GPR sensors known and the fea-
 ture maps of individual GPR images being calculated as ex-
 plained in Section 2, in this step, the corresponding feature
 maps are projected into this 3D volume based on the spatial
 configuration of different sensors. When the ground prediction

²OneVision, IDS, Pisa, Italy.

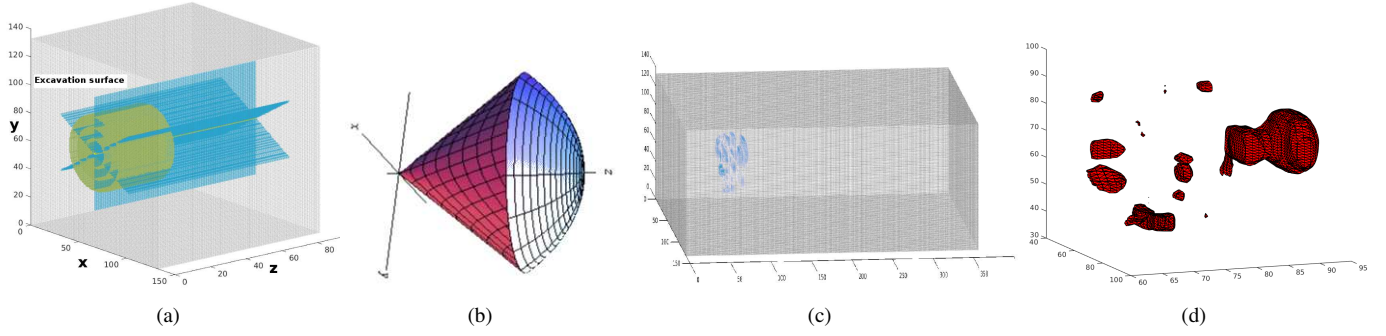


Figure 5: (a) Local 3D accumulator with origin located at the system centre. Three green circular planes show the scanning planes of GPR sensors on three radii; and the three blue planes show the locations of the seismic sensors; (b) Conical energy spreading: the locations related to a image pixel could be on a partial surface; (c) an example of the updated 3D accumulator in front of the prediction system; (d) an example of the extracted events from the 3D accumulator.

157 system moves forward, the anomalous feature map of new im-180
 158 ages will gradually add evidence into the 3D accumulator. The-181
 159 accumulator allows efficient accumulation of small amounts of-182
 160 information from individual sensor data and may provide more-183
 161 accurate and confident map of the front space. It also allows the-184
 162 extraction of probable events from the 3D volume based on the-185
 163 voxel values. This step is composed of four stages as explained-186
 164 below.

165 3.1. Discretization of the 3D space

166 As shown in Figure 5(a), the space ahead of the excavation 190
 167 surface is discretized into 3D voxel grids and used as a 3D ac- 191
 168 cumulator \mathbf{G} . The value of each voxel grid indicates its “pos- 192
 169 sibility” of being occupied by anomalous events. All the grids 193
 170 are initialized with value 0, $\mathbf{G} = 0$.

171 Let $x - y$ be the plane where all the GPR antennae are lo- 195
 172 cated; let z be the direction perpendicular to the $x - y$ plane 196
 and directing to the front of the excavation surface; let origin 197
 of the accumulator $(0, 0, 0)$ be the centre of the prediction sys-
 tem at the first scanning location. The size and resolution of the
 accumulator are defined by the characteristics of sensors (e.g.
 data resolution, effective penetrating range) and the distance
 between two consecutive scanning locations of the prediction
 system. The accumulator should cover the scanning area of all
 the subsystem sensors. Let the size of the 3D accumulator be
 (W, H, L) with resolution Δr_s ; there are $(i \times j \times k)$ grids in the
 accumulator, where

$$(i, j, k) \in \text{round}([W, H, L]/\Delta r_s) \quad (1)$$

171 A resolution of 0.1m is used in the following experiments to 201
 172 demonstrate the proposed method. 202

173 3.2. 3D accumulator updating

174 As explained previously in Section 1, the ground prediction 204
 175 system rotates in an anti-clockwise direction with a constant 205
 176 rate to collect data; and the data collection process repeats when 206
 177 the system moves forward. Given the radius R of a GPR scan- 207
 178 ning cross section (Figure 5(a)) and the starting scanning angle
 179 θ , each 2D pixel on the GPR image plane will contribute a set

of weighted “votes” to some 3D spatial locations in the 3D ac-
 cumulator. A pixel at location (x, z) on a 2D radar image³ or
 (x, D) (where $D = z \times \text{velocity}$ is the distance of the pixel to the
 scanning surface) can be projected to a location (X_{3d}, Y_{3d}, Z_{3d})
 in the 3D accumulator based on sensor locations and scanning
 directions, where $Z_{3d} = Z_0 + D$, (x_0, y_0, Z_0) is the location of the
 centre of the prediction system with respect to the origin in 3D.

187 When the radar energy travels in the ground, it spreads out in 187
 188 a conical projection, as shown in Figure 5(b), so a pixel (x, D) 188
 189 on a 2D radar image could be the reflection from all possible 189
 spatial locations on a partial sphere surface with radius D and
 centred at (X_{3d}, Y_{3d}, Z_{3d}) . For this reason, all the related voxel
 grids on this partial sphere are updated accordingly in the 3D
 accumulator. The size of the cone is dependent on the centre
 frequency of the radar energy, the depth of targets to the
 ground surface, and the average relative dielectric permittivity
 of ground in local area [17], e.g. higher frequency antennae
 usually have narrower propagation cones.

Let d be the distance between a voxel grid on the sphere
 and the related central voxel grid at (X_{3d}, Y_{3d}, Z_{3d}) , where $d \in$
 $[0, D \times \sin(\alpha/2)]$, and α is the angle of the propagation cone, the
 weights of different voxel grids on the sphere follows a Gaus-
 sian distribution with zero mean and $D \times \sin(\alpha/2)/3$ standard
 deviation, noted as:

$$p_d \sim \mathcal{N}(0, (\frac{D \times \sin(\alpha/2)}{3})^2) \quad (2)$$

198 All the related voxels on this partial sphere are updated accord- 198
 199 ingly by summing up the feature scores in I_{out} weighted by p_d 199
 200 in Equation 2. An example of the updated 3D accumulator is 200
 shown in Figure 5(c). The algorithm for 3D accumulator updat-
 201 ing is given in Algorithm 2. 202

203 3.3. Events extraction from 3D accumulator

204 After updating the accumulator with all the sensor data at a 204
 205 certain location (chainage in the tunnel), the voxel grids with 205
 206 high votes in the accumulator are extracted and grouped as po- 206
 207 tential events. Let $iso_{value} = \text{mean}(\mathbf{G}) + \text{std}(\mathbf{G})$, the voxel

³Note: the top-left corner is used as the origin on an image.

Algorithm 2 Updating 3D accumulator given the location of system centre (X_0, Y_0, Z_0) in the accumulator.

```

1:  $R = [r_1, r_2, r_3], \theta = [\theta_1, \theta_2, \theta_3]$ 
2: for each pixel  $(x, D)$  with value  $I_{x,z}$  in  $I_{out}$  do
3:   % find the location of each pixel in the 3D cell:
4:    $X_{3d} = Round(R \times \sin(\theta) / \Delta rrs) + X_0$ 
5:    $Y_{3d} = Round(R \times \cos(\theta) / \Delta s) + Y_0$ 
6:    $Z_{3d} = Round(D / \Delta rs) + Z_0$ 
7:   % find corresponding potential locations  $G_0$  on the
   sphere where
8:    $|G_0 - Z_0| < D + 0.1$  and  $d \in [0, D \times \sin(\alpha/2)]$ 
9:   % obtain the probability of different locations based on
   the weight defined by  $p_d$ :
10:   $d = |G_0 - (X_{3d}, Y_{3d})|, p_d \sim \mathcal{N}(0, (\frac{D \times \sin(\alpha/2)}{3})^2)$ 
11:  % update all related locations in the 3D accumulator
12:  for each location  $G_0$  on the sphere do
13:     $G_0 = G_0 + p_d \times I_{x,z}$ 
14:  end for
15: end for

```

grids in \mathbf{G} with higher values than $isoValue$ are kept. Then, the connected components are grouped as potential events based on three-dimensional 26-connected neighbourhood connectivity. Small isolated components (less than $(0.4/\Delta rs)^3$) are removed by counting the number of connected voxel grids in the component. Examples of the isolated events are shown in Figure 5 (d).

The extraction algorithm is presented in Algorithm 3. The detected 3D events are also re-projected onto individual sensor image planes as validated features (Figure 2 (b)); this method has the advantage of only keeping those image areas with high scores or regions detected by multiple sensors.

Algorithm 3 Events extraction from 3D accumulator \mathbf{G}

```

1: % threshold the 3D volume to keep certain voxels
2:  $isoValue = mean(\mathbf{G}) + std(\mathbf{G})$ 
3:  $vo \in \mathbf{G}$  and  $vo > isoValue$ 
4: % find connected regions in  $vo$ 
5:  $CC_{26}(vo) \leftarrow$  3D 26-connected neighbourhood
6: % remove small isolated regions in  $CC_{26}(vo)$ 
7:  $O_t :=$  regions with areas more than  $(0.4/\Delta rs)^3$ 
8: Return  $O_t$ 

```

3.4. Tracking of detected events at subsequent locations

Tracking of detected events means finding the correspondence between previously detected events and the latest detected events at a subsequent location(s). As the ground prediction system moves forward in the tunnel, it gets closer to the potential objects ahead and more information could be gathered by the imaging system. Tracking of detected 3D events can help to estimate the global size and nature of the events. Because events are extracted from the 3D accumulator, their absolute locations, including 3D centroids and bounding boxes, are used as the inputs of the tracking method.

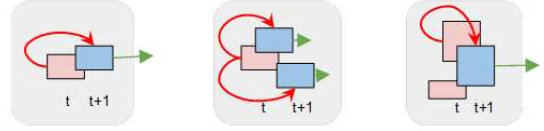


Figure 6: (Left) Simple scenario (no ambiguity): one event is connected with one event from previous frame; (Middle) Split: when multiple events at time $t + 1$ intersect with the same event at time t , they may relate to the different parts of an existing event and can be assigned the same *event id*; (Right) Nearest event (ambiguity): when one event at time $t + 1$ intersects with multiple events at time t , its nearest object at time t is chosen as the correspondence.

As shown in Figure 6 (a), if the bounding box of a detected event at location $t + 1$ (noted as o_{t+1}^j) intersects with the bounding box of any previously detected events at t (noted as o_t^i), the events pair $\{o_t^i \rightarrow o_{t+1}^j\}$ can be considered as corresponding events. Ambiguities may exist as shown in Figure 6 (b) and (c). The case in (b) is considered as an object split so the two latest events at $t + 1$ can both relate to the same event. For the case in (c), the event detected at time $t + 1$ is associated to its nearest object at time t based on the Nearest-Neighbour rule. An example side-view image of detected events is shown in Figure 7. After establishing the correspondences of tracked events, the global *event id* of previously detected events are propagated and assigned to the corresponding events at the subsequent locations. Information of the 3D events extracted at a certain location, including global *event id*, 3D location (centroid), size (bounding box), is stored in an event database for further analysis and visualisation to the user. Information of the corresponding re-projected 2D image features are also stored in the database.

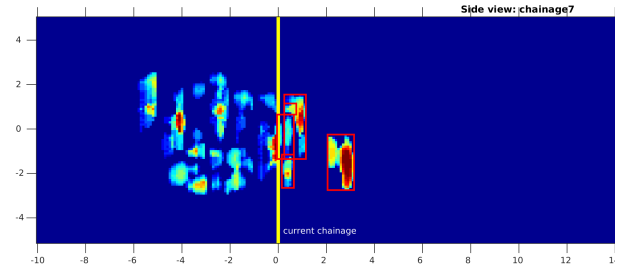


Figure 7: Example of detected events from multiple sets of GPR data (water inflow scenario as detailed in Section 4.2).

4. Experimental results

Test site set-up. A geophysical survey was conducted with the aforementioned ground prediction radar system in Park Forum, Eindhoven, (Netherlands) in 2015. Several scenarios representing the common hazards in tunnelling construction were simulated by burying objects in the ground. In order to simulate the tunnel forwarding process of a TBM where sensor measurements are concurrent with the ring construction operations, soil was replaced and compacted gradually at 7 levels. 0m level is at the top of the buried targets, and the distance between two consecutive levels is 1m. Sensor measurements were collected



(a) Water inflow scenario constructed using two water-filled tanks. (b) Karst scenario constructed using two polystyrene blocks.



(c) Mock-up of a circular multi-GPR system.

Figure 8: Simulation of two scenarios of hazards in tunnelling construction (Photo credit: IDS, NFM, Geo2X).

on each level and the acquired datasets are used to test the proposed event detection and tracking method. Images of the water inflow scenario and karst scenario are shown in Figure 8(a) and Figure 8(b).

GPR configuration. The GPR system was developed by IDS (Pisa, Italy) and consists of two high frequency antenna and one low frequency long range antenna with a control unit and a data storage system [11]. In order to simulate the circular data capturing process of GPR on a TBM, a mock-up GPR configuration was designed, composed of an axis driven into the soil to support an arm with two wheels on one side to turn around the centre. An encoder mounted on the front wheel counts the number of turns of the wheel to encode the position of the GPR along the perimeter. The GPR mock up is operated by two persons, one pulls it with a rope, the other pushes the mock-up towards the ground so that the wheel with the encoder always touches the ground (Figure 8(c)). The imaging system is placed on three different radii (1m, 1m80, 2m60) sequentially (along an arm), and on each radius the system is rotated in an anti-clockwise direction with a constant rate to collect data, so each GPR sensor can provide one data set per radius and 3 sensors can generate 9 images in total [12]. The proposed event detection/tracking method in this paper is flexible to the variations of GPR position set-up, which means the locations, number and frequencies of the GPR sensors could be changed based on users' demand. For example, in current experiment GPR data is captured at three different radii: 1m, 1m80, 2m60 with three sets of GPR antennae (a low frequency GPR and two high frequency GPR sensors), but more radii could be added if needed.

In the following sections, all the captured GPR images are marked by their: Level (distance from the top of the buried target to the surveyed surface): 0m, 1m, \dots , 6m; Radius: $R1(1m)$,

$R2(1.8m)$ and $R3(2.6m)$; and sensor: $S1$ (high-frequency GPR antenna 1), $S2$ (high-frequency GPR antenna 2) and $S3$ (low-frequency GPR).

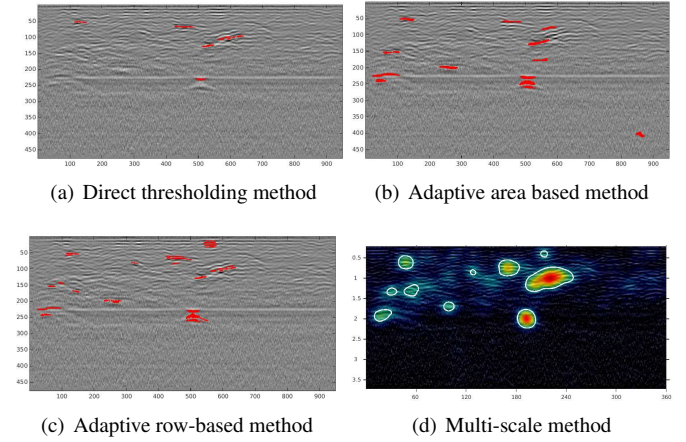


Figure 9: Examples of detected anomalous areas by different methods on the Karst scenario data set, at level-0m, radius 1m and from high-frequency sensor 1. Each image displayed is of 360° . In unit of y-axis in (a),(b),(c) is image pixel and the unit (d) is in metres.

4.1. Experimental results of extracted 2D anomalous areas

Three baseline methods were investigated for 2D anomalous areas detection (Table 1): a) **The direct thresholding method (DTM)** is based on global statistics of the amplitude in an GPR image. A threshold is automatically calculated for the whole image based on maximum entropy [18] and image pixels with higher values than the threshold are kept. Then, by counting the number of pixels in each connected component, clusters with fewer pixels than the threshold are considered as outliers and removed. However, as the energy levels of the top part and the bottom part of the image may not be equal (even after gain correction), a global threshold may risk missing objects further away from the top. b) **The adaptive row-based thresholding method (ARTM)** is used to threshold the image based on the image intensity in different time-slice windows. By vertically scanning the radar image, a local threshold is calculated for each local region (every nr rows), the scores of each pixel are accumulated and the pixels with low scores are removed. Based on the average energy in a local area in the radar image, area reflectivity method is a measure of the clutter in the corresponding surveyed area that may relate to the presence of pebbles, fractures, etc. c) **The adaptive area reflectivity method (AARM)** is used to adaptively find the areas with large average reflectivity in different time-slice windows. It combines the row-based thresholding method and the area-based method by accumulating the areas with large reflectivity in each time-slice window. An average filter with size 10×10 pixels is applied on each input image to calculate the average area reflectivity in each time-slice window; then the direct thresholding method in [18] is applied on this image to find interesting pixels (relating to areas in the original image).

Some experimental results are shown in Figure 9 and Figure 10. Compared with the direct thresholding method, the

Baseline methods	Processing steps
Direct thresholding method (DTM)	A global intensity threshold is computed for each input image based on the method of maximum entropy thresholding [18]; then, pixels are grouped as connected clusters and the clusters with small number of pixels are considered as outliers and removed.
Adaptive row-based thresholding method (ARTM)	This method thresholds an image based on the image intensity in different time-slice windows. Each image is scanned from top to bottom every ns rows and the following nr rows are considered being in a time-slice window. For each step, a local threshold is computed for the window using direct thresholding method and the score of each pixel (i.e., noted as 1 if it is above the threshold; otherwise, noted as 0) is accumulated as the window moves from top to bottom. Pixels with low scores are removed.
Adaptive area reflectivity method (AARM)	This method is to adaptively find the areas with large average reflectivity in different time-slice windows. It combines the row-based thresholding method and the area-based method by accumulating the areas with large reflectivity in each time-slice window.

Table 1: Three baseline methods for anomalous area extraction from 2D GPR data.

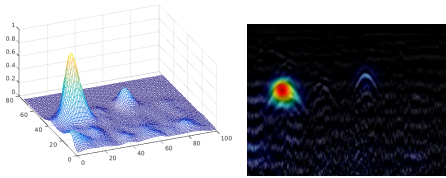


Figure 10: An example of anomalous image features detection from GPR B-scan images.

adaptive area reflectivity and row-based thresholding methods are more suitable for detecting areas with high reflectivity at different depths. Outputs of the adaptive row-based method and the multi-scale method are similar to each other but the latter is also able to consider the texture information and can detect regions with relatively weak intensities.

4.2. Experimental results of the “Water inflow” scenario.

The water inflow scenario, as seen in Figure 8(a), was constructed using 2 plastic tanks filled with water. The final target is 5m long, 0.5m wide and 1.6m deep, the top of the target is at level 0m and seven groups of sensor data were captured every 1m on top of the target by gradually filling in materials vertically built up the ground. The top-view of the buried tank and the sensor configurations is shown in Figure 12 (Left). The data acquisition on each radius starts from the 0 degree line (displayed in orange colour). In Figure 11(a), the intersection of the buried water tank and the scanning cross section of radius 1m is displayed, where x-axis indicates the angular location of the antenna from the starting edge and y-axis indicates the depth in metres. It can be seen that the buried target is located around 120° and 300°. In Figure 11(b-f), the GPR images and their corresponding anomalous areas from three different GPR sensors at radius 1m, level 0m and level 1m are displayed. As seen in the images captured at 1m level, the most anomalous image area are shown when sensors are on top of the buried water tanks, and these areas are all correctly detected by the proposed method in Figure 11(b-d). For images captured at 1m

level and farther away (Figure 11(e,f)), only the low-frequency antenna (sensor 3) can identify part of the water tank and the reflections from the water tank are distinguishable around 120°. By integrating the image detections from different sensors, the top-view of the detected events is shown in Figure 12(right).

4.3. Experimental results of the “Karst scenario”

The karst scenario was simulated by burying 2 packs of polystyrene blocks (4m length, 1m wide and 0.5m thick) at 1.5m depth and gradually adding soil on top of the blocks (Figure 8(b)). The top-view configurations of the buried polystyrene blocks is shown in Figure 13(a). Theoretically, they should be detected by the antennae at 0°, 180° and 360°, as shown in Figure 14(a). Examples of GPR images and the detected anomalous areas are shown in Figure 14. It can be seen that the reflections from the buried target were picked up by the presented method as anomalous areas. After integrating the image detections from different sensors, the detected event is shown in Figure 13 (right).

Discussion. In the above experiment, specific objects were buried in the ground as targets, which is different from real construction site. In a real tunnel construction site, the ground could be more heterogeneous than the designed test site (N.B. it could also be less heterogeneous as the ground isn’t disturbed in real construction sites). For example, more ground water could appear in the real test site, so the GPR data quality may not be good enough for anomalous feature detection. The remedy for this is to add another type of imaging sensors on TULIPS based on the seismic signals, which has already been addressed by Pawan et al. in [19]. Another challenge in real construction site might be that different types of targets may intertwine with each other and the sensor data could be very noisy (large and dense scattering), so the proposed method may not be able to distinguish different targets. Although the GPR data used in the above experiment is from a specifically built test site with clayed soil, the proposed method in this paper does not have any presumptions of the type of surrounding soils although the signal should be strong enough for penetrating the ground.

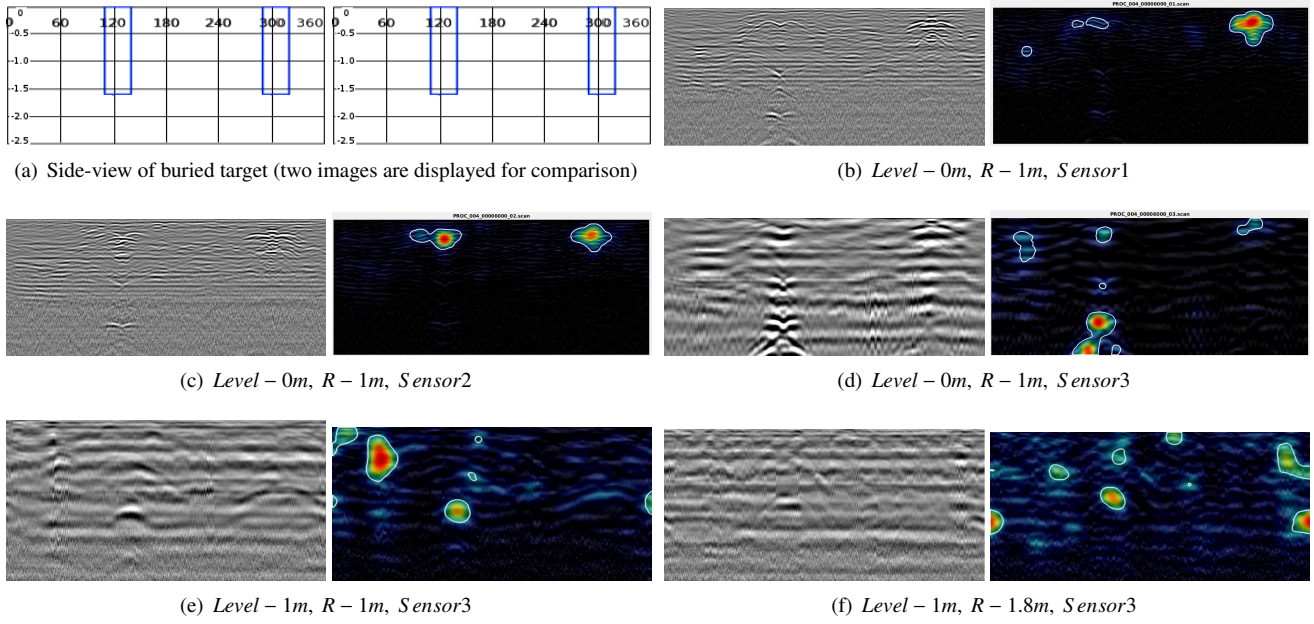


Figure 11: Experimental results of the water inflow scenario: comparison of the anomalous areas detected from different GPR images with the ground truth. (a) Intersection of the water tanks and the scanning cross section. x -axis: 0 - 360° degree, y -axis: depth (0.5m for each grid). (b-f) Processing results of different sensor data captured at different levels. "Level" stands for the distance between the GPR antenna to the top of the buried target. The water tanks can be well seen by all antennas at level 0m at a radius of 1m and $1\text{m}80$ from the centre.

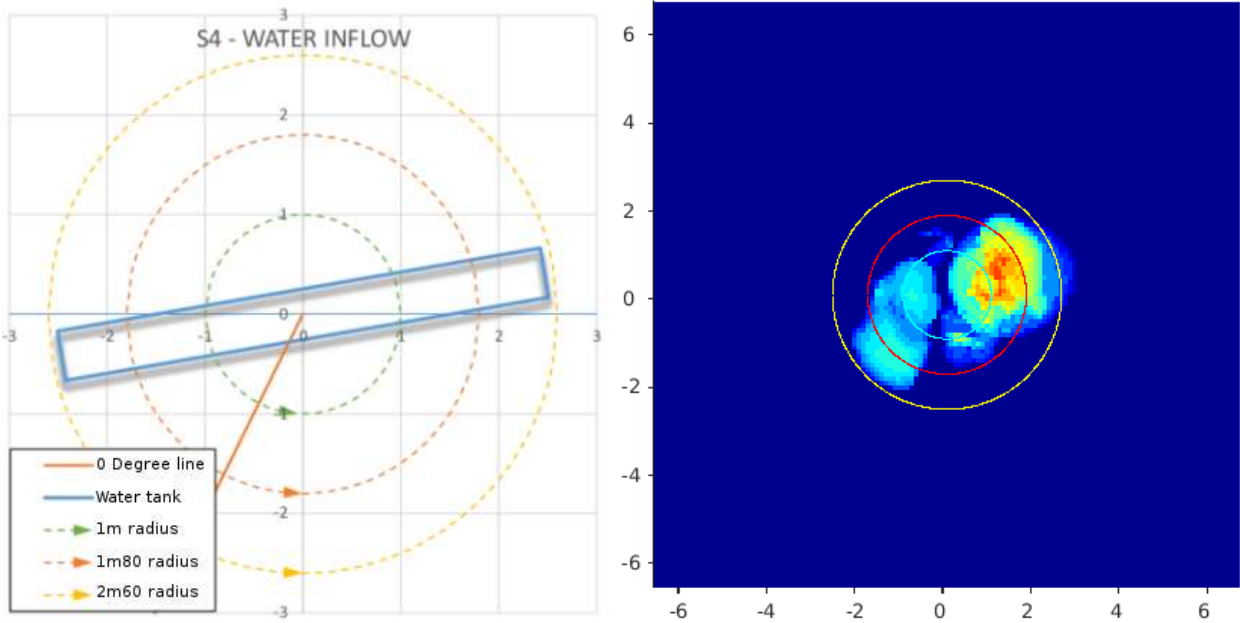


Figure 12: Top-view of the water inflow scenario. (Left) Sketch of the buried water tanks and the sensor configuration, (right) top-view of the reconstructed buried targets using GPR data at level 0m .

393 5. Conclusion

394 This paper has presented a method for anomalous event de-
 395 tect and tracking in a tunnel look-ahead ground prediction
 396 system with multiple ground penetrating radars. Anomalous
 397 areas are detected from individual GPR images and the inte-

398 gration of multiple sets of sensor data can help recover the 3D
 399 location of the probable events in front of the excavation sur-
 400 face. The proposed methods were evaluated with two sets of
 401 data captured at a specifically built test field with buried tar-
 402 gets, and the experimental results show that the buried targets
 403 can be correctly detected from the sensor data using the pro-

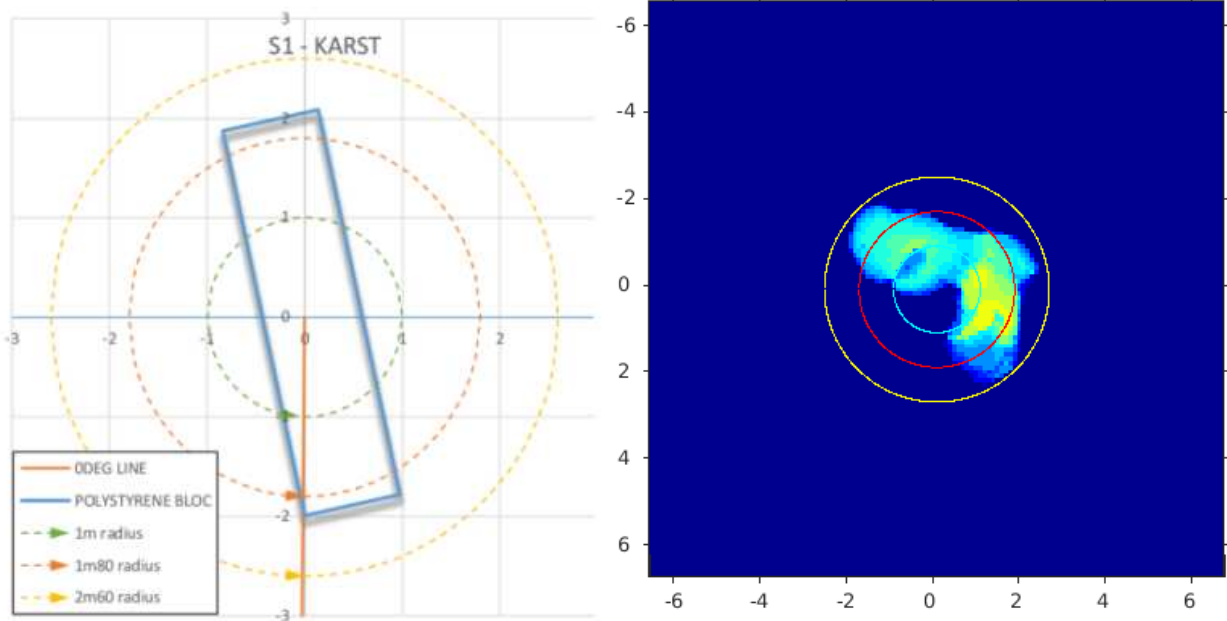


Figure 13: Top-view of the karst scenario. (Left) Sketch of the buried polystyrene blocks and the sensor configuration; (right) top-view of the predicted events from radar images on three radii at level 0m.

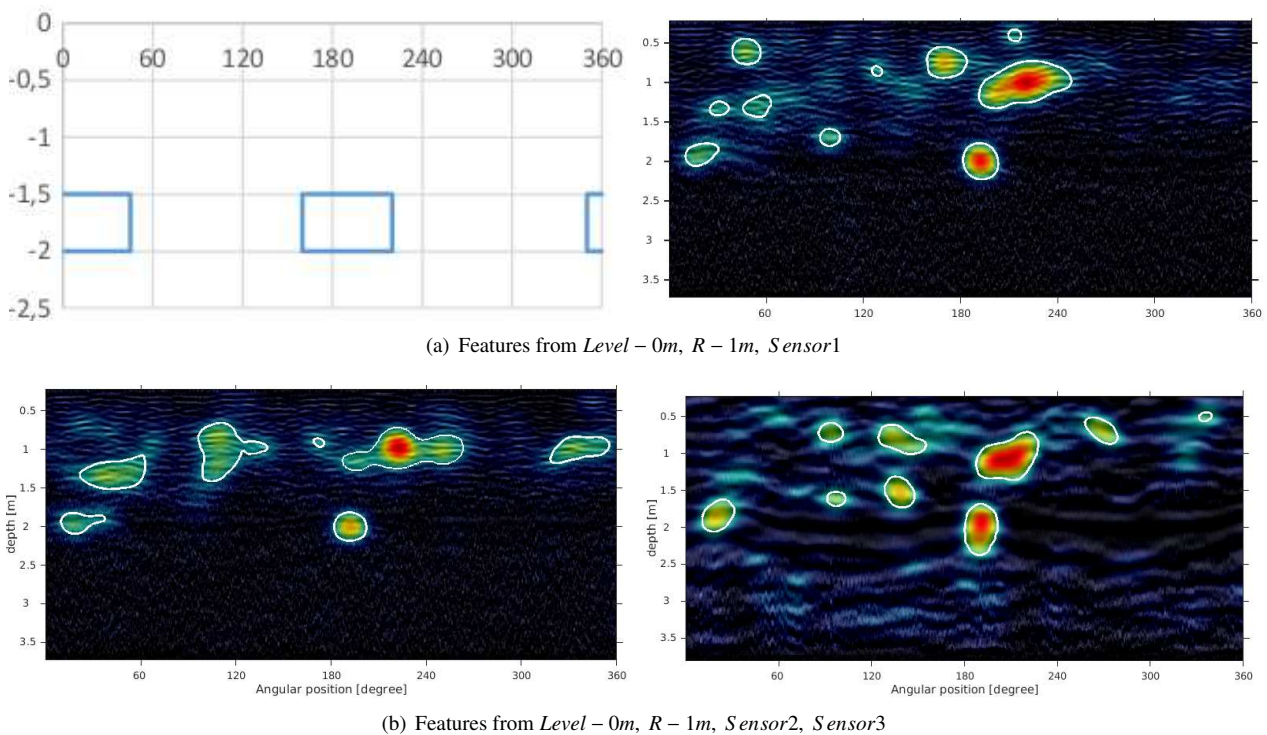


Figure 14: Experimental results of the karst scenario: comparison of the anomalous areas detected from different GPR B-scan images with the ground truth.

404 posed method. The detected 3D events and the corresponding
 405 2D image areas (features) are stored in a back-end feature and
 406 event database. For future work, after gathering a large col-
 407 lection of real tunnel cases with the ground prediction system,
 408 including the sensor prospecting imaging data, the geological

sketch, geological hazards, TBM parameters, geological condi-
 tions (as-built events) revealed by excavation, and geo-experts'
 interpretation, alternative methods could be developed to pre-
 dict the type of anomalous events and to combine the seismic
 and GPR data using advanced machine learning methods to fur-

414 ther improve the reliability of the prediction results.

415 Acknowledgements

416 We gratefully acknowledge the financial support of the EU
417 under Grant Agreement 280712. We thank the project partners
418 in GEO2X and IDS for providing the sensor data used in this
419 paper. We also thank the project manager, Thomas Camus, for
420 his tireless efforts in coordinating the project.

- 421 [1] Y. Zheng, Q. Zhang, J. Zhao, Challenges and opportunities of using tunnel
422 boring machines in mining, *Tunnelling and Underground Space Technol-*
423 *ogy* 57 (2016) 287 – 299.
- 424 [2] S.-S. Leu, T. J. W. Adi, Probabilistic prediction of tunnel geology using
425 a hybrid neural-hmm, *Engineering Applications of Artificial Intelligence*
426 24 (2011) 658 – 665.
- 427 [3] Z. Guan, T. Deng, S. Du, B. Li, Y. Jiang, Markovian geology predic-
428 tion approach and its application in mountain tunnels, *Tunnelling and*
429 *Underground Space Technology* 31 (2012) 61 – 67.
- 430 [4] S. Li, S. Li, Q. Zhang, Y. Xue, B. Liu, M. Su, Z. Wang, S. Wang, Pre-
431 dicting geological hazards during tunnel construction, *Journal of Rock*
432 *Mechanics and Geotechnical Engineering* 2 (2010) 232 – 242.
- 433 [5] S. Li, J. Song, J. Zhang, C. Wang, B. Liu, F. Liu, S. Ma, L. Nie, A new
434 comprehensive geological prediction method based on constrained inver-
435 sion and integrated interpretation for water-bearing tunnel structures, *Eur-*
436 *opean Journal of Environmental and Civil Engineering* 21 (2017) 1441–
437 1465.
- 438 [6] A. Alimoradi, A. Moradzadeh, R. Naderi, M. Z. Salehi, A. Etemadi, Pre-
439 diction of geological hazardous zones in front of a tunnel face using tsp-
440 203 and artificial neural networks, *Tunnelling and Underground Space*
441 *Technology* 23 (2008) 711 – 717.
- 442 [7] J. Park, K.-H. Lee, J. Park, H. Choi, I.-M. Lee, Predicting anomalous zone
443 ahead of tunnel face utilizing electrical resistivity: I. algorithm and mea-
444 suring system development, *Tunnelling and Underground Space Tech-*
445 *nology* 60 (2016) 141 – 150.
- 446 [8] A. K. Benson, Applications of ground penetrating radar in assessing some
447 geological hazards: examples of groundwater contamination, faults, cavi-
448 ties, *Journal of Applied Geophysics* 33 (1995) 177 – 193.
- 449 [9] X. Núñez-Nieto, M. Solla, A. Novo, H. Lorenzo, Three-dimensional
450 ground-penetrating radar methodologies for the characterization and vol-
451 umetric reconstruction of underground tunneling, *Construction and*
452 *Building Materials* 71 (2014) 551 – 560.
- 453 [10] S. Li, B. Liu, X. Xu, L. Nie, Z. Liu, J. Song, H. Sun, L. Chen, K. Fan, An
454 overview of ahead geological prospecting in tunneling, *Tunnelling and*
455 *Underground Space Technology* 63 (2017) 69 – 94.
- 456 [11] A. Simi, G. Manacorda, The NeTTUN project: Design of a GPR antenna
457 for a TBM, in: 16th International Conference on Ground Penetrating
458 Radar (GPR), pp. 1–6.
- 459 [12] X. Wang, S. Sun, J. Wang, A. Yarovoy, B. Neduczka, G. Manacorda, Real
460 GPR signal processing for target recognition with circular array anten-
461 nas, in: 2016 URSI International Symposium on Electromagnetic Theory
462 (EMTS), pp. 818–821.
- 463 [13] Q. Dou, L. Wei, D. R. Magee, A. G. Cohn, Real-time hyperbola recogni-
464 tion and fitting in gpr data, *IEEE Transactions on Geoscience and Remote*
465 *Sensing* 55 (2017) 51–62.
- 466 [14] J. Harel, C. Koch, P. Perona, Graph-based visual saliency, in: *Proceedings*
467 *of the 19th International Conference on Neural Information Processing*
468 *Systems, NIPS’06, MIT Press, Cambridge, MA, USA, 2006*, pp. 545–
469 552.
- 470 [15] L. Itti, C. Koch, E. Niebur, A model of saliency-based visual attention for
471 rapid scene analysis, *IEEE Transactions on Pattern Analysis and Machine*
472 *Intelligence* 20 (1998) 1254–1259.
- 473 [16] A. Goldman, I. Cohen, Anomaly detection based on an iterative local
474 statistics approach, in: *23rd IEEE Convention of Electrical and Electron-*
475 *ics Engineers in Israel*, pp. 440–443.
- 476 [17] L. Conyers, *Ground-penetrating Radar for Archaeology, Geophysical*
477 *methods for archaeology, AltaMira Press, 2004*.
- 478 [18] J. Kapur, P. Sahoo, A. Wong, A new method for gray-level picture thresh-
479 olding using the entropy of the histogram, *Computer Vision, Graphics,*
480 *and Image Processing* 29 (1985) 273 – 285.

- 481 [19] P. Bharadwaj, G. Drijkoningen, W. Mulder, J. Thorbecke, B. Neduczka,
482 R. Jenneskens, A shear-wave seismic system using full-waveform inver-
483 sion to look ahead of a tunnel-boring machine, *Near Surface Geophysics*
484 15 (2017) 210 – 224.